

The imprint of $f(R)$ gravity on weak gravitational lensing I: Connection between observables and large-scale structure

Yuichi Higuchi^{1*} and Masato Shirasaki²

¹*Astronomy Data Center, National Astronomical Observatory of Japan, 2-21-1 Osawa, Mitaka, Tokyo 181-8588, Japan*

²*Division of Theoretical Astronomy, National Astronomical Observatory of Japan, 2-21-1 Osawa, Mitaka, Tokyo 181-8588, Japan*

Accepted 4/5/2016. Received 3/3/2016; in original form 3/3/2016

ABSTRACT

We study the effect of $f(R)$ gravity on the statistical properties of various large-scale structures which can be probed in weak gravitational lensing measurements. A set of ray-tracing simulations of gravitational lensing in $f(R)$ gravity enables us to explore cosmological information on (i) stacking analyses of weak lensing observables and (ii) peak statistics in reconstructed lensing mass maps. For the $f(R)$ model proposed by Hu & Sawicki, the measured lensing signals of dark matter haloes in the stacking analysis would show a $\lesssim 10\%$ difference between the standard Λ CDM and the $f(R)$ model when the additional degree of freedom in $f(R)$ model would be $|f_{R0}| \sim 10^{-5}$. Among various large-scale structures to be studied in stacking analysis, troughs, i.e. underdensity regions in projected plane of foreground massive haloes, could be promising to constrain the model with $|f_{R0}| \sim 10^{-5}$, while stacking analysis around voids is found to be difficult to improve the constraint of $|f_{R0}|$ even in future lensing surveys with a sky coverage of ~ 1000 square degrees. On the peak statistics, we confirm the correspondence between local maxima and dark matter haloes along the line of sight, regardless of the modification of gravity in our simulation. Thus, the number count of high significance local maxima would be useful to probe the mass function of dark matter haloes even in the $f(R)$ model with $|f_{R0}| \lesssim 10^{-5}$. We also find that including local minima in lensing mass maps would be helpful to improve the constraint on $f(R)$ gravity down to $|f_{R0}| = 10^{-5}$ in ongoing weak lensing surveys.

Key words: gravitational lensing; weak, large-scale structure of Universe

1 INTRODUCTION

The standard cosmological model called Λ CDM model has been established by various astronomical observations such as measure of distance to supernovae, spatial distribution of galaxies and cosmic microwave background (e.g., [Perlmutter et al. 1997](#); [Tegmark et al. 2006](#); [Planck Collaboration et al. 2015](#)). Although the Λ CDM model is consistent with observational results within the statistical uncertainty, the physical origin of accelerating expansion of the Universe is still uncertain. At present, there exist two physical models to explain the cosmic acceleration at redshift of $z \lesssim 1$: dynamical dark energy model and modified gravity theory. The former would realize the accelerating expansion of the Universe within the theory of general relativity by introducing unknown energy, while the latter does not require an exotic form of energy but modify the basic equation of gravitational action. In order to distinguish these two scenarios, the measurement of gravitational growth of cosmic matter density would be essential because the modification of gravity could induce some specific features in matter density distribution in the Universe.

Vainshtein ([Vainshtein 1972](#)) or chameleon mechanisms ([Khoury & Weltman 2004a,b](#); [Brax et al. 2004](#)) are among the most interesting features in modified gravity theory, which would guarantee the success of general relativity in the solar system. However, modification of gravity can affect the evolution of matter density distribution on extragalactic scales. For

* E-mail: yuichi.higuchi@nao.ac.jp

instance, several N -body simulations indicate the modification of gravity would affect properties of group or cluster-sized haloes (Li & Hu 2011; Arnold et al. 2014; Hammami et al. 2015). In particular, the recent simulation in Aчитouv et al. (2015) showed that matter densities of haloes at central regions can increase up to 40% in some cases. Furthermore, the modification should give prominent effects on low density regions such as cosmic voids in which screening mechanisms do not work. Therefore, the differences of properties in low density regions have been investigated in previous numerical simulations (Li et al. 2012a; Zivick et al. 2015; Aчитouv et al. 2015). N -body simulations of modified gravity showed that the number count of voids defined in the spatial distribution of haloes would be about 2 times smaller than that in general relativity, while the matter density around voids would show a difference with a level of a few percent (Cai et al. 2015). While numerical simulations have been advanced of understanding the statistical properties of cosmic matter density in modified gravity, some of those properties in simulations are based on three-dimensional matter density distribution and thus cannot be observed in actual observations directly. Therefore, it is important to investigate *how the imprint of modified gravity on cosmic matter density would appear in real observables*. Among various observables, we would focus on weak gravitational lensing effect on galaxies in imaging surveys.

Gravitational lensing is an unbiased probe of the matter distribution in the Universe. Small image distortions of distant galaxies are caused by intervening mass distribution. Small distortion caused by the large-scale structure of the Universe is called cosmic shear. It contains, in principle, rich information on the matter distribution at small and large scales and the evolution over time. Image distortion induced by gravitational lensing is, however, very small in general. Therefore, we need statistical analyses of the cosmic shear signal by sampling a large number of distant galaxies in order to extract cosmological information from gravitational lensing. Ongoing and future galaxy imaging surveys are aimed at measuring projected matter distribution over several thousand square degrees and the averaged matter distribution around possible large-scale structures such as galaxies, galaxy clusters and cosmic voids. Clearly, we need to understand the relation between cosmic matter density and the lensing observables when examining the modified gravity with galaxy imaging surveys.

In this paper, we perform ray-tracing simulation of gravitational lensing in the modified gravity and explore the relation between large-scale structures and the lensing observables in galaxy imaging surveys under the modification of gravity. In comparison with the recent study in Tessore et al. (2015), we properly take into account the deflection of light ray along the line of sight in our gravitational lensing simulations. We consider the two observables to reveal the matter density distribution in the Universe with weak gravitational lensing: the stacked lensing signals around various large-scale structures and the peak statistics on reconstructed mass distribution from cosmic shear. The former observables are related with the average matter density distribution around dark matter haloes and cosmic voids. In addition, we also focus on the peak statistics to extract cosmological information on the abundance of large-scale structures.

This paper is organized as follows. In Section 2, the cosmological model is described. In Section 3, we summarize basics of weak lensing and analysis methods used in this paper. We also explain details of our lensing simulation and the definition of large-scale structures in Section 4. In Section 5, we provide results of our lensing analysis in numerical simulation of modified gravity and compare the results of modified gravity model and the Λ CDM model in detail. Conclusions and discussions are summarized in Section 6.

2 COSMOLOGICAL MODEL

There exist various extensions to the standard Λ CDM model. Here, we consider competing models called $f(R)$ models, which represents cosmological models with modified gravity. This model can explain the observed cosmic acceleration at $z \lesssim 1$ and satisfy the solar system tests with appropriate parameters. Throughout this paper, we assume a spatially flat universe and adopt the cosmological parameters which follow the result with Planck satellite (Planck Collaboration et al. 2015): matter density $\Omega_{m0} = 0.315$, dark energy density $\Omega_{\Lambda 0} = 0.685$, Hubble parameter $h = 0.673$ and the scalar spectral index $n_s = 0.945$.

$f(R)$ model

In $f(R)$ model, the Einstein-Hilbert action is modified by a general function of the scalar curvature R (Nojiri & Odintsov 2011; Li et al. 2012b; Shi et al. 2015),

$$S_G = \int d^4x \sqrt{-g} \left[\frac{R + f(R)}{16\pi G} \right]. \quad (1)$$

The action with Eq. (1) leads the modified Einstein equation as

$$G_{\mu\nu} + f_R R_{\mu\nu} - \left(\frac{f}{2} - \square f_R \right) g_{\mu\nu} - \nabla_\mu \nabla_\nu f_R = 8\pi G T_{\mu\nu}, \quad (2)$$

where $f_R \equiv df/dR$, $G_{\mu\nu} \equiv R_{\mu\nu} - 1/2g_{\mu\nu}R$ and $\square \equiv \nabla^\alpha \nabla_\alpha$. Assuming a Friedmann-Robertson-Walker (FRW) metric, one can determine the time evolution of the Hubble parameter in $f(R)$ model as follows:

$$H^2 - f_R \left(H \frac{dH}{d \ln a} + H^2 \right) + \frac{f}{6} + H^2 f_{RR} \frac{dR}{d \ln a} = \frac{8\pi G}{3} \rho_m. \quad (3)$$

One can also consider the evolution of matter density perturbations in $f(R)$ model. For sub-horizon modes ($k \gtrsim aH$) in the quasi-static limit¹, the linear growth of matter density perturbation is determined by (e.g., [Bean et al. 2007](#))

$$\frac{d^2 g_+}{da^2} + \left(\frac{3}{a} + \frac{1}{H} \frac{dH}{da} \right) \frac{dg_+}{da} - \frac{3\tilde{\Omega}_{m0} a^{-3}}{(H/H_0)^2 (1+f_R)} \frac{1-2Q}{2-3Q} \frac{g_+}{a^2} = 0, \quad (4)$$

where $\tilde{\Omega}_{m0}$ is the effective matter density at present time. We can specify this effective density $\tilde{\Omega}_{m0}$ as

$$H_{f(R)} = H_0 \sqrt{\tilde{\Omega}_{m0} a^{-3} + \tilde{\Omega}_{DE} \exp \left[-3 \int_1^a da' (1 + \tilde{w}_{DE}(a'))/a' \right]}, \quad (5)$$

where $H_{f(R)}$ is given by Eq. (3). Note that $\tilde{\Omega}$ and \tilde{w}_{DE} are equivalent to Λ CDM model for small $|f_{R0}|$. The function Q in Eq. (4) is given by

$$Q(k, a) = -2 \left(\frac{k}{a} \right)^2 \frac{f_{RR}}{1+f_R}. \quad (6)$$

Note that the function of Q induces the non-trivial scale dependence of the linear growth rate $g_+(k, a) = D(k, a)/a$ in $f(R)$ model, while the linear growth rate is exactly a function of a in General Relativity.

In this paper, we will consider the representative example of $f(R)$ models as proposed in [Hu & Sawicki \(2007\)](#) (hereafter denoted as HS model),

$$f(R) = -2\Lambda \frac{R^n}{R^n + \mu^{2n}}, \quad (7)$$

where Λ , μ and n are free parameters in this model. For $R \gg \mu^2$, one can approximate the function of $f(R)$ as follows:

$$f(R) = -2\Lambda - \frac{f_{R0}}{n} \frac{\bar{R}_0^{n+1}}{R^n}, \quad (8)$$

where \bar{R}_0 is defined by the present scalar curvature of the background space-time and $f_{R0} = -2\Lambda\mu^2/\bar{R}_0^2 = f_R(\bar{R}_0)$. In the HS model with $|f_{R0}| \ll 1$, the background expansion would be almost equivalent to one in Λ CDM model. In practice, for $|f_{R0}| \ll 10^{-2}$, geometric tests such as distance measurement with supernovae could not distinguish between the HS model and the Λ CDM model ([Martinelli et al. 2012](#)). Nevertheless, measurements of gravitational growth would be helpful to constrain on HS model due to the scale dependence of growth rate as shown in Eq. (4). Furthermore, the non-linear gravitational growth in the HS model have been studied with cosmological N -body simulations ([Oyaizu et al. 2008](#); [Schmidt et al. 2009](#); [He et al. 2013](#); [Zhao 2014](#)). Such previous works indicate that statistics of galaxy groups or clusters provide meaningful information about the modification of gravity. Therefore, combination of statistics between weak lensing and galaxy clusters are among the interesting probes of the HS model. In the following, we focus on the case of $n = 1$.

3 WEAK LENSING

3.1 Basics

We here summarize basics of weak gravitational lensing effects. When considering the observed position of a source object as $\boldsymbol{\theta}$ and the true position as $\boldsymbol{\beta}$, one can characterize the distortion of image of a source object by the following 2D matrix

$$A_{ij} = \frac{\partial \beta^i}{\partial \theta^j} \equiv \begin{pmatrix} 1 - \kappa - \gamma_1 & -\gamma_2 - \omega \\ -\gamma_2 - \omega & 1 - \kappa + \gamma_1 \end{pmatrix}, \quad (9)$$

where κ is convergence, γ is shear and ω is rotation.

Let us consider the case of General Relativity. One can relate each component of A_{ij} to the second derivative of the gravitational potential as follows ([Bartelmann & Schneider 2001](#))

$$A_{ij} = \delta_{ij} - \Phi_{ij}, \quad (10)$$

$$\Phi_{ij} = \frac{2}{c^2} \int_0^x d\chi' q(\chi, \chi') \partial_i \partial_j \Phi(\chi'), \quad (11)$$

$$q(\chi, \chi') = \frac{r(\chi - \chi')r(\chi')}{r(\chi)}, \quad (12)$$

¹ [de La Cruz-Dombriz et al. \(2008\)](#); [Bose et al. \(2015\)](#) have shown that the quasi-static approximation becomes quite reasonable for models with $|f_{R0}| \ll 1$ today.

where χ is the comoving distance and $r(\chi)$ represents the comoving angular diameter distance. Gravitational potential Φ can be related to matter density perturbation δ through Poisson equation. Therefore, convergence can be expressed as the weighted integral of δ along the line of sight

$$\kappa = \int_0^{\chi_s} W_\kappa(\chi, \chi_s) \delta, \quad (13)$$

where χ_s is comoving distance to source galaxies and $W_\kappa(\chi)$ is the lensing weight function defined as

$$W_\kappa(\chi, \chi_s) = \frac{3}{2} \left(\frac{H_0}{c} \right)^2 \Omega_{m0} q(\chi_s, \chi) (1 + z(\chi)). \quad (14)$$

In general, the lensing equation would be governed by so-called lensing potential $(\Phi + \Psi)/2$ where Φ and Ψ are the Bardeen potentials appeared in metric perturbation in the Newtonian gauge. The lensing potential in $f(R)$ gravity would be governed by the Poisson equation in General relativity, making Eqs. (10), (11) and (13) available in the HS model with $|f_{R0}| \ll 1$. Therefore, equations for gravitational lensing in $f(R)$ gravity become the same as in general relativity (Arnold et al. 2014).

3.2 Statistical Analysis

While reduced shear $g_i = \gamma_i/(1-\kappa)$ can be estimated from the ellipticity of galaxy (e.g., Schneider & Seitz 1995; Bartelmann & Schneider 2001), the intrinsic shape would be dominated in the measured ellipticity of individual galaxy in typical ground-based imaging surveys. Therefore, we need to perform statistical analyses with a large number of source galaxies. Here, we introduce two statistical methods to study the large-scale structures with weak lensing measurement.

3.2.1 Stacked lensing

Stacking analysis of weak lensing observables is a powerful method to study the average matter density distribution around an object of interest.

For a given tracer of large-scale structures (LSS), we define a stacked signal as

$$\langle \gamma_+ \rangle(\theta) = \langle n_{\text{LSS}}(\phi) \gamma_+(\theta + \phi) \rangle, \quad (15)$$

where n_{LSS} represents the number density of the tracer. The stacked signal can be related to the surface excess of convergence as (Bartelmann & Schneider 2001)

$$\langle \gamma_+ \rangle(\theta) = \bar{\kappa}(\theta) - \langle \kappa \rangle(\theta), \quad (16)$$

where $\langle \kappa \rangle$ denotes the azimuthal average profile of convergence and $\bar{\kappa}(\theta)$ is a mean convergence value within a circular aperture of radius θ defined as

$$\bar{\kappa}(\theta) = \frac{1}{\pi\theta^2} \int_{\phi < \theta} d^2\phi \kappa(\phi). \quad (17)$$

In order to constrain on the nature of gravity with LSS, it is essential to study the lower density regions in the Universe. Since any modified gravity theories should pass the existing robust tests of General relativity in the solar system or the high density region in the Universe, an extra fifth force in the modified gravity model might be weak but not completely disappeared. Therefore, the matter density distribution in the Universe would be affected by the fifth force in more efficient way at lower density regions (e.g., Li et al. 2012a; Clampitt et al. 2013; Cai et al. 2015). Also, the matter fluctuation at linear scales can be a promising target to seek for the signature of modification of general relativity because the linear growth rate would be dependent on the length scale as shown in Eq. (4). The linear growth rate can be measured by stacked signals around galaxies or clusters of galaxies at large angular separations (e.g., Oguri & Takada 2011).

Hence, we consider three tracers of LSS, named voids, troughs, and haloes in the present paper. Voids are commonly defined by empty regions or extremely low density regions in the Universe. Gruen et al. (2016) has recently proposed a new tracer of low density regions in the Universe, which is called trough. Troughs are defined as underdense regions in the projected galaxy distributions. Under the assumption that galaxy would be the biased tracer of matter distribution in a three-dimensional space, troughs would be an effective tracer of matter density distributions with $\delta < 0$. Haloes are the counterpart of voids, showing the high contrast of matter density with the typical value of $\delta \gtrsim 100$. We examine whether the stacked signal around voids or troughs (the tracers of underdensity regions) can be affected by the extra fifth force in $f(R)$ model. On the other hand, we study the stacked signals around haloes at large scales to explore the scale-dependency of linear growth rate. In the following, we summarize the model of stacked lensing signal around haloes, voids and troughs.

Haloes

We here describe the model of the lensing observable $\langle\gamma_+\rangle$ around dark matter haloes. Let us suppose that a density profile of a host halo is described by the universal NFW profile (Navarro et al. 1997),

$$\rho_h(r) = \frac{\rho_s}{(r/r_s)(1+r/r_s)^2}, \quad (18)$$

where ρ_s and r_s are a scale density and a scale radius, respectively. The parameters ρ_s and r_s can be essentially convolved into one parameter, the concentration $c_{\text{vir}}(M, z)$, by the use of two halo mass relations; namely, $M_{\text{vir}} = 4\pi r_{\text{vir}}^3 \Delta_{\text{vir}}(z) \rho_{\text{crit}}(z)/3$, where r_{vir} is a virial radius corresponding to the overdensity criterion $\Delta_{\text{vir}}(z)$ (as shown in, e.g., Navarro et al. 1997), and $M_{\text{vir}} = \int dV \rho_h(\rho_s, r_s)$ with the integral performed out to r_{vir} . In this paper, we adopt the functional form of the concentration parameter in Dutton & Macciò (2014),

$$\log_{10} c_{\text{vir}}(M, z) = 0.537 + 0.488 \exp(-0.718z^{1.08}) + (-0.097 + 0.024z) \log_{10} \left(\frac{M}{2 \times 10^{12} h^{-1} M_{\odot}} \right). \quad (19)$$

For a given halo sample with the mass range of $M_{\text{min}} < M < M_{\text{max}}$ and the redshift range of $z_{\text{min}} < z < z_{\text{max}}$, one can find stacked signals around dark matter haloes are expressed as (e.g., Marian et al. 2015)

$$\langle\gamma_+\rangle(\theta) = \int \frac{d^2\ell}{(2\pi)^2} P_{h\kappa}(\ell) J_2(\ell\theta), \quad (20)$$

where $P_{h\kappa}(\ell)$ represents the halo-convergence cross power spectrum and $J_2(x)$ is the second-order Bessel function. In this paper, we apply the halo-model approach to model $P_{h\kappa}$. As follows in Oguri & Takada (2011); Shirasaki et al. (2016), the halo-convergence cross power spectrum spectrum is given by

$$P_{h\kappa}(\ell) = P_{h\kappa}^{1h}(\ell) + P_{h\kappa}^{2h}(\ell), \quad (21)$$

$$P_{h\kappa}^{1h}(\ell) = \frac{1}{\bar{n}_{\text{halo}}} \int_{z_{\text{min}}}^{z_{\text{max}}} dz \frac{d^2V}{dzd\Omega} \int_{M_{\text{min}}}^{M_{\text{max}}} dM \frac{dn}{dM} \frac{(1+z)^3}{\bar{\rho}_m(z)} \frac{W_{\kappa}(\chi, \chi_s)}{r(\chi)^2} \tilde{\rho}_h \left(k = \frac{\ell}{r(\chi)} \middle| z(\chi), M \right), \quad (22)$$

$$P_{h\kappa}^{2h}(\ell) = \frac{1}{\bar{n}_{\text{halo}}} \int_{z_{\text{min}}}^{z_{\text{max}}} dz \frac{d^2V}{dzd\Omega} \left[\int_{M_{\text{min}}}^{M_{\text{max}}} dM \frac{dn}{dM} b_h(z, M) \right] \frac{W_{\kappa}(\chi, \chi_s)}{r(\chi)^2} P_m^L \left(k = \frac{\ell}{r(\chi)}, z(\chi) \right), \quad (23)$$

where the volume element is expressed as $d^2V/dzd\Omega = \chi^2/H(z)$ for a spatially flat universe, $\tilde{\rho}_h$ represents the Fourier transform of Eq. (18), dn/dM and b_h denote the halo mass function and the linear halo bias, respectively. In Eqs. (22) and (23), \bar{n}_{halo} represents the average number density of haloes which is defined by

$$\bar{n}_{\text{halo}} = \int_{z_{\text{min}}}^{z_{\text{max}}} dz \frac{d^2V}{dzd\Omega} \int_{M_{\text{min}}}^{M_{\text{max}}} dM \frac{dn}{dM}. \quad (24)$$

In the case of the standard Λ CDM model, we adopt the model of halo mass function and linear halo bias with the overdensity of $\Delta = 200$ developed in Tinker et al. (2008, 2010). To remain consistent with our calculation, we convert the mass of the host halo using the definition of Δ as shown in Hu & Kravtsov (2003).

Voids

We next consider stacked lensing signals around voids. For the standard Λ CDM model, dark matter density profile of voids have been investigated in previous studies (e.g. Sheth & van de Weygaert 2004; Pan et al. 2012). Both theoretical and observational studies have indicated that a matter density would be almost constant over an underdense region and there exists a very sharp spike called a ridge at the edge of voids. These features are found in the N -body simulation of $f(R)$ gravity but the inner profile of voids would be affected by the modification of gravity (e.g. Cai et al. 2015).

In order to make a simple void model which includes the properties found in the previous works, we consider a spherically symmetric void model called a double top-hat model (Higuchi et al. 2013). In this model, mass density of a given void is expressed as

$$\rho_v(r) = \begin{cases} \rho_1 & (r \leq R_1) \\ \rho_2 & (R_1 < r \leq R_2) \\ 0 & (R_2 < r) \end{cases}, \quad (25)$$

where r is a distance from the center of void, ρ_1 and ρ_2 are constant in each region. Assumed that the total mass between the void region ($r \leq R_1$) and the ridge region ($R_1 < r \leq R_2$) should be compensated each other, the density contrast of void is given by

$$\begin{aligned} \delta_v(r) &= \rho_v/\bar{\rho}_m - 1 \\ &= \begin{cases} \delta_1 & (r \leq R_1) \\ \delta_1 [1 - (R_2/R_1)^3]^{-1} & (R_1 < r \leq R_2) \\ 0 & (R_2 < r) \end{cases}, \end{aligned} \quad (26)$$

where we introduce the parameter of $\delta_1 = \rho_1/\bar{\rho}_m - 1$ and $\bar{\rho}_m$ represents the mean matter density. The corresponding shear profile from Eq. (26) can be calculated analytically as

$$\begin{aligned} \gamma_+(\theta) = & W_\kappa(\chi_l, \chi_s)\chi_l \frac{\delta_1}{3\theta^2} \left[\frac{1}{1 - (\theta_2/\theta_1)^3} \left\{ (\theta_2/\theta_1)^3 (2\theta_1^2 + \theta^2) \sqrt{\theta_1^2 - \theta^2} - (2\theta_2^2 + \theta^2) \sqrt{\theta_2^2 - \theta^2} \right\} \Theta(\theta_1 - \theta) \right. \\ & \left. - \frac{(2\theta_2^2 + \theta^2) \sqrt{\theta_2^2 - \theta^2}}{1 - (\theta_2/\theta_1)^3} \Theta(\theta - \theta_1)\Theta(\theta_2 - \theta) \right], \end{aligned} \quad (27)$$

where χ_l is the comoving distance to void, θ_i is defined by R_i/χ_l and $\Theta(x)$ represents the Heaviside step function.

Troughs

Troughs have been recently proposed in Gruen et al. (2016) as tracers of underdense regions in the Universe. In this paper, we define the trough with a given dark matter halo catalog. Let us consider a halo catalog with the selection function of $W_{\text{halo}}(z, M)$. For a given W_{halo} , the three-dimensional number density of haloes is defined by

$$n_{\text{halo},3D}(\mathbf{x}) = \sum_i^{N_{\text{halo}}} \delta^{(3)}(\mathbf{x} - \mathbf{x}_i) W_{\text{halo}}(z_i, M_i), \quad (28)$$

where N_{halo} represents the total number of haloes in the field of view. In this paper, we simply consider the functional form of $W_{\text{halo}}(z, M)$ as

$$W_{\text{halo}}(z, M) = \begin{cases} 1 & \text{for } z_{\text{min}} \leq z \leq z_{\text{max}} \text{ and } M \geq M_T \\ 0 & \text{others} \end{cases}, \quad (29)$$

where M_T is a selection criterion for halo mass. From the halo catalog, we can define the smoothed, projected number density of haloes as

$$G(\boldsymbol{\theta}) = \sum_{i=1}^{N_{\text{halo}}} W_T(|\boldsymbol{\theta} - \boldsymbol{\theta}_i|) W_{\text{halo}}(z_i, M_i), \quad (30)$$

where $W_T(x)$ is the weighted function to construct the smoothed density field and set to be the top-hat function as

$$W_T(|\boldsymbol{\theta} - \boldsymbol{\theta}_i|) = \begin{cases} 1/\pi\theta_T^2 & \text{for } |\boldsymbol{\theta} - \boldsymbol{\theta}_i| < \theta_T \\ 0 & \text{others} \end{cases}, \quad (31)$$

where θ_T represents the radius of the filter function. In the following, we call θ_T as trough radius. The positions of troughs are then selected by the points below the α -th percentile G_α of the distribution of $G(\boldsymbol{\theta})$.

As shown in the above selection of troughs, the statistical property of troughs would be governed by the new random field as

$$\delta_T(\boldsymbol{\theta}) = \int d^2\theta' W_T(|\boldsymbol{\theta} - \boldsymbol{\theta}'|) \delta_{\Sigma,h}(\boldsymbol{\theta}'), \quad (32)$$

where $\delta_{\Sigma,h}$ represents the contrast of the projected number density of haloes. Assumed that the probability P of finding N haloes at a given position of $\boldsymbol{\theta}$ can be determined by the value of $\delta_T(\boldsymbol{\theta})$, we can identify the expectation value of δ_T for a given N as

$$\langle \delta_T | N \rangle = \int_{-1}^{\infty} d\delta_T p(\delta_T | N), \quad (33)$$

where $p(\delta_T | N)$ represents the conditional probability distribution function of δ_T for a given N . Note that the Bayes' theorem tells

$$p(\delta_T | N) = \frac{P(N|\delta_T)P(\delta_T)}{P(N)}, \quad (34)$$

$$P(N) = \int_{-1}^{\infty} d\delta_T P(N|\delta_T)P(\delta_T). \quad (35)$$

Therefore, the maximum number of haloes within trough radius N_{max} should be determined by

$$\sum_{N=0}^{N_{\text{max}}} P(N) = \alpha, \quad (36)$$

for a given α to define the position of trough.

Gruen et al. (2016) proposed a simple model of the stacked signal around troughs under the following assumptions:

• The three-dimensional halo density field $n_{\text{halo},3\text{D}}$ can be described as a deterministic, biased tracer of the matter density field. This means that the projected matter density contrast δ_{Σ} within the redshift range of the halo catalog is equivalent to $\delta_{\Sigma,h}$.

- The random field $\delta_T(\boldsymbol{\theta})$ and the convergence field $\kappa(\boldsymbol{\theta})$ follow a Gaussian distribution.
- The probability of $P(N|\delta_T)$ is given by a biased Poisson process with the halo bias of \bar{b} .

Under these assumptions, we can calculate the azimuthally averaged convergence profile around troughs. Let K_i to be the average of convergence field over a distance of $\theta = [\theta_i, \theta_{i+1}]$ from the trough center, i.e.,

$$K_i = \frac{1}{\pi(\theta_{i+1}^2 - \theta_i^2)} \int_{A_i} d^2\theta' \kappa(\boldsymbol{\theta}'), \quad (37)$$

where A_i represents the i -th annuli around the trough. The average K_i over the position of troughs is then given by

$$\langle K_i | N_{\text{max}} \rangle = \frac{\text{Cov}(K_i, \delta_T) \sum_{N=0}^{N_{\text{max}}} P(N) \langle \delta_T | N \rangle}{\sigma_T^2 \sum_{N=0}^{N_{\text{max}}} P(N)}, \quad (38)$$

where σ_T^2 is the variance of δ_T and $\text{Cov}(K_i, \delta_T)$ is the covariance between K_i and δ_T . We refer the reader to [Gruen et al. \(2016\)](#) for the function form of $P(N)$ and the derivation of $\text{Cov}(K_i, \delta_T)$ and σ_T^2 . Hence, one can calculate the stacked signal around troughs by using Eqs. (16) and (38).

3.2.2 Peak Statistics

Reconstruction of smoothed convergence

In addition to stacked lensing, weak lensing provides a physical method to reconstruct the projected matter density field. The reconstruction is commonly based on the smoothed map of cosmic shear. Let us first define the smoothed convergence map as

$$\mathcal{K}(\boldsymbol{\theta}) = \int d^2\phi \kappa(\boldsymbol{\theta} - \boldsymbol{\phi}) U(\boldsymbol{\phi}), \quad (39)$$

where U is the filter function to be specified below. We can calculate the same quantity by smoothing the shear field γ as

$$\mathcal{K}(\boldsymbol{\theta}) = \int d^2\phi \gamma_+(\boldsymbol{\phi} : \boldsymbol{\theta}) Q_+(\boldsymbol{\phi}), \quad (40)$$

where γ_+ is the tangential component of the shear at position $\boldsymbol{\phi}$ relative to the point $\boldsymbol{\theta}$. The filter function for the shear field Q_+ is related to U by

$$Q_+(\boldsymbol{\theta}) = \int_0^\theta d\theta' \theta' U(\theta') - U(\theta). \quad (41)$$

We consider Q_+ to be defined with a finite extent. In this case, one finds

$$U(\theta) = 2 \int_\theta^{\theta_o} d\theta' \frac{Q_+(\theta')}{\theta'} - Q_+(\theta), \quad (42)$$

where θ_o is the outer boundary of the filter function.

In the following, we consider the truncated Gaussian filter (for U) as

$$U(\theta) = \frac{1}{\pi\theta_G^2} \exp\left(-\frac{\theta^2}{\theta_G^2}\right) - \frac{1}{\pi\theta_o^2} \left[1 - \exp\left(-\frac{\theta_o^2}{\theta_G^2}\right)\right], \quad (43)$$

$$Q_+(\theta) = \frac{1}{\pi\theta^2} \left[1 - \left(1 + \frac{\theta^2}{\theta_G^2}\right) \exp\left(-\frac{\theta^2}{\theta_G^2}\right)\right], \quad (44)$$

for $\theta \leq \theta_o$ and $U = Q_+ = 0$ elsewhere. Throughout this paper, we adopt $\theta_G = 1$ arcmin and $\theta_o = 10$ arcmin. Note that this choice of θ_G is considered to be an optimal smoothing scale for the detection of massive galaxy clusters using weak lensing for $z_{\text{source}} = 1.0$ ([Hamana et al. 2004](#)).

The local maxima or minima found in a smoothed convergence map would have cosmological information originated from massive dark matter haloes, voids, and the superposition of large scale structures (e.g., [Hamana et al. 2004](#); [Dietrich & Hartlap 2010](#); [Kratovichil et al. 2010](#); [Yang et al. 2011](#); [Shirasaki et al. 2016](#)). In this paper, we define peaks in the convergence map by finding the local maxima or minima. Peak height is in practice normalized as $\nu(\boldsymbol{\theta}) = \mathcal{K}(\boldsymbol{\theta})/\sigma_{\text{shape}}$ where σ_{shape} is the noise variance coming from intrinsic ellipticity of galaxies. We estimate σ_{shape} as follows

$$\sigma_{\text{shape}}^2 = \frac{\sigma_e^2}{2n_{\text{gal}}} \int_0^{\theta_{\text{out}}} d\theta Q_+^2(\theta), \quad (45)$$

where σ_e is the rms value of intrinsic ellipticity of galaxies and n_{gal} is the number density of galaxies. We assume $\sigma_e = 0.4$ and $n_{\text{gal}} = 30 \text{ arcmin}^{-2}$ which are typical values for ground-based imaging surveys.

High significance local maxima and their abundance

On a smoothed lensing map, local maxima with high signal-to-noise ratio would be likely caused by galaxy clusters (Hamana et al. 2004). We thus locate high- ν local maxima on a convergence map and associate each of them with an isolated massive halo along the line of sight. Supposed that the universal NFW density profile (Eq. 18), we can calculate the convergence profile κ_h for a given halo analytically (Hamana et al. 2004).

In order to predict peak heights in a convergence map, we adopt the simple assumption that each peak position is exactly at the halo center. Under this assumption, the peak height in absence of shape noise is given by

$$\mathcal{K}_{\text{peak},h} = \int d^2\phi U(\phi; \theta_G, \theta_o) \kappa_h(\phi). \quad (46)$$

The actual peak height on a noisy convergence map is determined not by Eq. (46), but by a probability distribution function (Fan et al. 2010). The probability distribution function of the measured peak height $\mathcal{K}_{\text{peak,obs}}$ with a given $\mathcal{K}_{\text{peak},h}$ is denoted by $\text{Prob}(\mathcal{K}_{\text{peak,obs}}|\mathcal{K}_{\text{peak},h})$ in this paper. The detailed functional form of $\text{Prob}(\mathcal{K}_{\text{peak,obs}}|\mathcal{K}_{\text{peak},h})$ is found in Shirasaki et al. (2015).

We identify local maxima in a smoothed lensing map and match each peak with a massive dark matter halo along the line of sight. The simple peak count is useful to extract the information of the abundance of massive clusters. One can select the lensing peaks by its peak height. For a given threshold of peak height ν_{thre} , one can predict the surface number density of peaks with $\nu > \nu_{\text{thre}}$ as follows (Hamana et al. 2004):

$$N_{\text{peak}}(> \nu_{\text{thre}}) = \int dz dM \frac{d^2V}{dzd\Omega} \frac{dn}{dM} S(z, M|\nu_{\text{thre}}). \quad (47)$$

where $S(z, M|\nu_{\text{thre}})$ expresses the selection function of weak lensing selected clusters for a given threshold of ν_{thre} . It is given by

$$S(z, M|\nu_{\text{thre}}) = \int_{\nu_{\text{thre}}\sigma_{\text{shape}}}^{\infty} d\mathcal{K}_{\text{peak,obs}} \text{Prob}(\mathcal{K}_{\text{peak,obs}}|\mathcal{K}_{\text{peak},h}(z, M)). \quad (48)$$

4 SIMULATION

In order to study the relation of weak lensing statistics with the underlying large-scale structures, we perform the ray-tracing simulation of gravitational lensing with a set of N -body simulations.

4.1 N -body and Ray-tracing simulations

We first run a N -body simulation to generate a three-dimensional matter density field. We use the adaptive mesh refinement code ECOSMOG for a wide class of modified gravity (Li et al. 2012b). The simulation volume has a comoving box length of $240 h^{-1}\text{Mpc}$, resolved using a uniform 512^3 root grid and 7 levels of mesh refinement, implying a maximum comoving spatial resolution of $3.6 h^{-1}\text{kpc}$. We proceed the mesh refinement when the effective particle number in a grid cell would be larger than 8. The density assignment and force interpolation in a cell is performed by the triangular shaped cloud (TSC) method. We generate the initial conditions using a parallel code `mpggraphic` developed by Prunet et al. (2008). The initial redshift is set to $z_{\text{init}} = 85$, where we compute the linear matter transfer function using `linger` (Bertschinger 1995). In simulations, we adopt the following cosmological parameters : matter density $\Omega_{\text{m}0} = 0.315$, dark energy density $\Omega_{\Lambda 0} = 0.685$, Hubble parameter $h = 0.673$ and the scalar spectral index $n_s = 0.945$. For the HS model, we consider two models with $|f_{\text{R}0}| = 10^{-5}$ and 10^{-6} , referred as F5 and F6, respectively. Note that we can safely set $\tilde{w}_{\text{DE}} = -1$ and $\nabla(\Psi + \Phi)/2 = 4\pi G\bar{\rho}_m\delta a^2$ in the model with $|f_{\text{R}0}| \ll 1$.

For ray-tracing simulations of gravitational lensing, we generate light-cone outputs using multiple simulation boxes in the following manner. Our simulations are placed to cover the past light-cone of a hypothetical observer with an angular extent $5^\circ \times 5^\circ$, from $z = 0$ to 1, similar to the methods in White & Hu (2000), Hamana & Mellier (2001), and Sato et al. (2009). Details of the configuration are found in the last reference. The angular grid size of our maps is $5^\circ/4096 \sim 0.075$ arcmin. For a given cosmological model, we first store particle data of N -body simulation at various redshifts. We then randomly shift the simulation boxes in order to avoid the same structure appearing multiple times along a line-of-sight. In total, we generate 100 independent lensing maps with the source redshift of $z_{\text{source}} = 1$ from our N -body simulation. Figure 1 shows an example of our simulated convergence map for different cosmological models. Although it is difficult to distinguish with three models by eyes, the lensing statistics would enable us to clarify the differences among these. In Figure 2, we compare the convergence power spectrum for three cosmological models. The points with error bar represent the simulation results for the Λ CDM model and the HS model with $|f_{\text{R}0}| = 10^{-5}$ and 10^{-6} . The green and blue solid lines correspond to the theoretical model of convergence power spectrum for the case of $|f_{\text{R}0}| = 10^{-5}$ and 10^{-6} , respectively. Under the Limber approximation

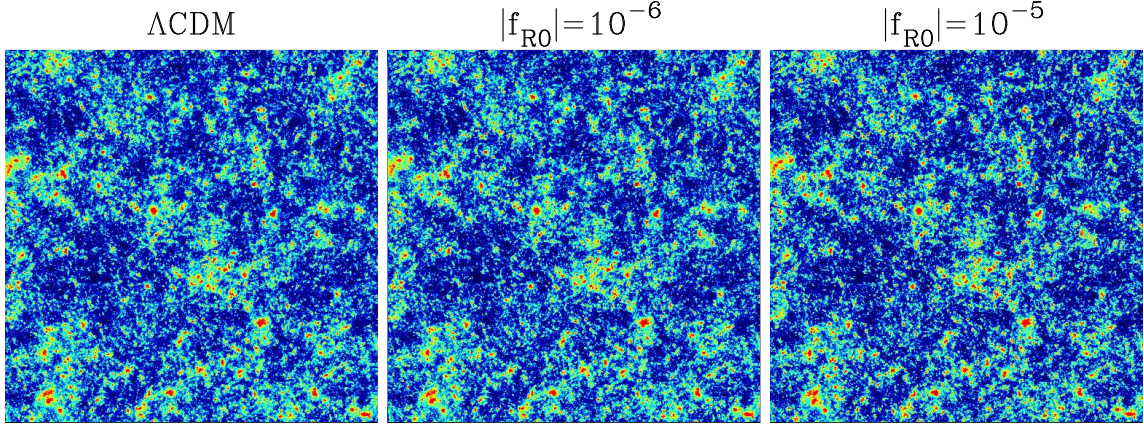


Figure 1. Convergence map for three different cosmological models. The source redshift is set to be unity. Each map covers 5×5 square degrees. It is difficult to distinguish the differences among three maps by eyes.

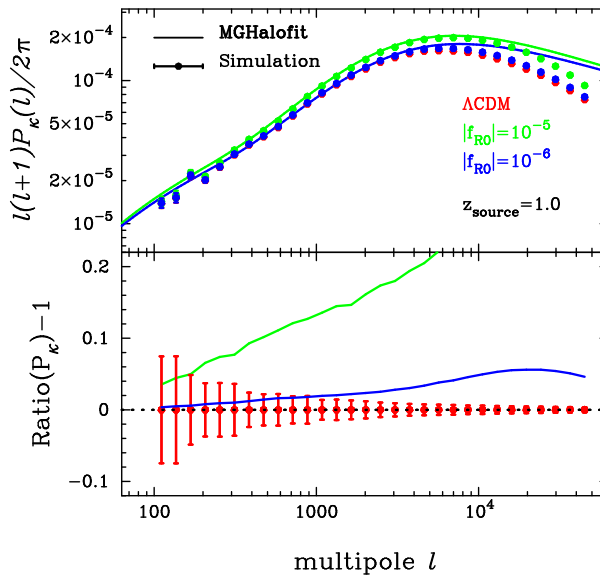


Figure 2. Convergence power spectrum for three different models. In the top panel, the coloured points with error bar show the average power spectrum over 100 realizations of lensing maps. The coloured solid line represents the theoretical model of power spectrum with the fitting formula of the non-linear matter power spectrum (Zhao 2014). In the bottom panel, we show the difference between the HS model and the fiducial Λ CDM model obtained from our simulation. In both panels, the error bar corresponds to the standard deviation of the mean estimated from 100 maps.

(Limber 1954; Kaiser 1992) and Eq. (13), one can calculate the convergence power spectrum as

$$P_\kappa(\ell) = \int_0^{\chi_s} d\chi \frac{W_\kappa(\chi, \chi_s)^2}{r(\chi)^2} P_\delta \left(k = \frac{\ell}{r(\chi)}, z(\chi) \right), \quad (49)$$

where $P_\delta(k)$ is the three dimensional matter power spectrum. For the non-linear power spectrum of matter density P_δ , we adopt the fitting formula called MGHalofit (Zhao 2014). According to Figure 2, our lensing simulation is found to be consistent with previous modified gravity simulations.

4.2 Definition of Large-Scale Structures

haloes

In each output of the N -body simulation, we locate dark matter haloes using the standard friend-of-friend (FOF) algorithm with the linking parameter of $b = 0.2$. We define the mass of each halo by the spherical overdensity mass with $\Delta = 200$, which is denoted by M_{200} . The position of each halo is defined by the position of the particle located at the potential maximum in each FOF group. In the following analysis, we use haloes with a mass M_{200} greater than $10^{13} h^{-1} M_\odot$. Using the FOF haloes,

we construct mock group catalogs on the light cone by arranging the simulation outputs in the same manner as the ray-tracing simulation. We mark the positions of the haloes in the lensing map. In summary, our mock catalogs contain data about the masses, redshifts, and angular positions on the lensing map for the haloes.

Voids

In order to define void in each realization, we employ the public code `Void Finder` (Foster & Nelson 2009) on the void finding algorithm developed by Hoyle & Vogeley (2004) and Hoyle et al. (2005). It finds small number density regions of haloes and make spheres. Then, radius of those spheres are enlarged and spheres are marginalized with marginalization criteria. We adopt the same parameters found in Foster & Nelson (2009) except for the minimum radius ξ . We use $\xi = 10$ Mpc as the minimum radius of voids. The number count of voids does not strongly depend on this value for voids whose radius are more than 15 Mpc (Higuchi et al. 2013). When running the `Void Finder`, we use haloes at $0.15 \leq z \leq 0.65$ with masses larger than $M_{200} \geq 10^{13} h^{-1} M_{\odot}$. In order to select legitimate voids, we select voids whose centers are more than the effective radius of voids away from the edges of simulation boxes.

Troughs

In this paper, we define trough as centers of cylindrical regions with low number density of haloes as summarized in Section 3.2.1. In order to define positions of troughs, we count the number count in each cylinder $G(\theta)$ and then select the set of trough positions as the points below the 20th percentile of the distribution of $G(\theta)$. In our study, we estimate the number count for the circles spaced by 0.75 arcmin. For the selection, we set $z_{\min} = 0.2$ and $z_{\text{high}} = 0.6$, while we examine the three mass threshold cases for $M_T = 10^{13} h^{-1} M_{\odot}$, $5 \times 10^{13} h^{-1} M_{\odot}$ and $10^{14} h^{-1} M_{\odot}$. Furthermore, we study the dependence of the trough radius on our results by considering $\theta_T = 5, 10, 20$ and 30 arcmin.

5 RESULTS

In the following, we summarize the results on our lensing analyses with 100 ray-tracing simulations.

5.1 Stacked Lensing

5.1.1 haloes

We perform the stacked analysis around haloes by selecting their masses and redshifts. We consider the three redshift bins of $0.1 \leq z \leq 0.3$, $0.3 \leq z \leq 0.5$, and $0.5 \leq z \leq 0.7$ and three mass bins of $10^{13} h^{-1} M_{\odot} \leq M_{200} < 10^{13.5} h^{-1} M_{\odot}$, $10^{13.5} h^{-1} M_{\odot} \leq M_{200} < 10^{14} h^{-1} M_{\odot}$ and $10^{14} h^{-1} M_{\odot} \leq M_{200} < 10^{15} h^{-1} M_{\odot}$. In the stacking analysis, we measure the azimuthally averaged, logarithmically spaced radial profile of tangential shear in the radial range of $\theta = 1 - 100$ arcmin around the center of each cluster and then stack the shear profiles over the haloes found in each realization. The typical number of haloes in the stacking analysis ranges from 40 to 2000 in each realization.

We start to compare the result obtained from 100 simulations for Λ CDM with the halo model as in Section 3.2.1. The left panel in Figure 3 summarizes the stacked tangential shear profiles in each mass and redshift bin. The black point in the left panel corresponds to the average values of tangential shear over 100 realizations and the error bar represents the standard deviation of the average tangential shear (i.e. the standard deviation over 100 realizations divided by $\sqrt{100}$). We also show the theoretical model as shown in Section 3.2.1 by the red lines. We have confirmed that our simulation results for the standard Λ CDM model are in good agreement with the halo model prediction for the range of $\theta = 1 - 100$ arcmin.

We then consider the comparison of tangential shear between $f(R)$ gravity and Λ CDM. In order to clarify the differences, we introduce the ratio of tangential shear between two cases. The right panel in Figure 3 shows the ratio of tangential shear over three mass and redshift bins. In the right panel, the red line corresponds to the ratio between the F5 model and Λ CDM, while the green line is for the F6 model. The gray error bars in the right panel represent the standard deviation of tangential shear for $|f_{R0}| = 0$. According to the right panel in Figure 3, there are found no differences between the stacked signal for the F6 and Λ CDM model over the wide range of halo masses and redshifts. On the other hand, the differences from the Λ CDM model are clearly found in the case of the F5 model. Interestingly, we find the significant deviation of the stacked signal at $\theta \leq \theta_{200}$, where θ_{200} is the corresponding angular radius of $R_{200} = (3M_{200}/4\pi 200\bar{\rho}_m)^{1/3}$. This effect might be caused by the different mass assembly history in $f(R)$ cosmology from the standard model, although the further investigation would be required. Note that the recent numerical study has reported that $f(R)$ gravity would induce the changes of the three-dimensional halo density profile (Zhao et al. 2011; Aчитouv et al. 2015), while mass-concentration relation in F6 are found to be negligible for haloes with masses larger than $10^{13} h^{-1} M_{\odot}$ for all redshift (Shi et al. 2015). We also find that the stacked signal at the transition scale between the one-halo and two halo terms would be affected by the modification of gravity. The

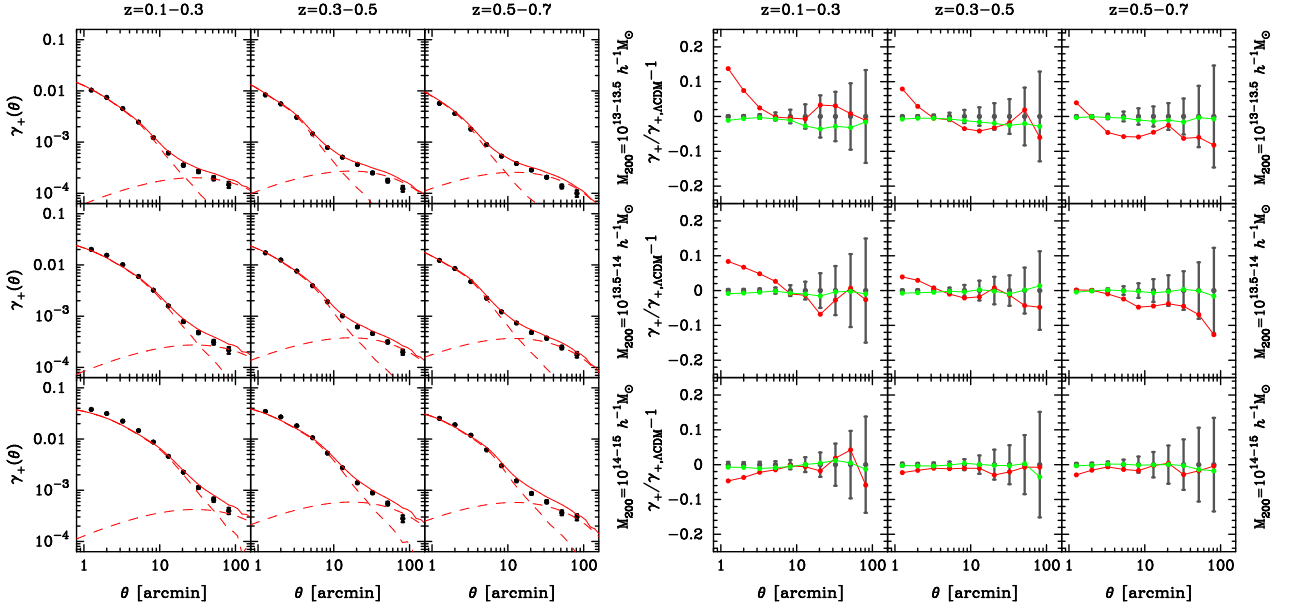


Figure 3. Stacked profile of haloes. We divide the haloes by their halo masses and redshifts. *Left:* The result for the standard Λ CDM model. The black point with error bar shows the result obtained from 100 ray-tracing simulations, while the red solid line shows the corresponding halo-model prediction as shown in Section 3.2.1. The two red dashed lines are the one-halo and two-halo terms, respectively. *Right:* The comparison of results with $f(R)$ gravity and Λ CDM. The each panel shows the ratio of stacked signal between the case of $f(R)$ gravity and Λ CDM model. The red line shows the case of $|f_{R0}| = 10^{-5}$, while the green one is for $|f_{R0}| = 10^{-6}$. The gray error bars represent the standard deviation of ensemble average of stacked signals over 100 realizations.

trend of effects of $f(R)$ gravity on stacked profile shows the complex dependences of the halo masses and redshifts. We have confirmed that the three-dimensional halo density profile ρ_h shows the similar trend as shown in Figure 3 when we stacked ρ_h for each halo mass and redshift bin, i.e., more concentrated halo profile tends to make the tangential shear larger at $\theta \lesssim \theta_{200}$ and vice versa.

5.1.2 Voids

We next consider the stacked signals around voids. In the stacked analysis, we divide the voids by their radius obtained from the **Void Finder**. We consider two radius bins of $20 - 30 h^{-1}\text{Mpc}$ and $30 - 40 h^{-1}\text{Mpc}$. Note that the total number of voids over 100 realizations is found to be ~ 1000 . This means that we can find only ~ 10 voids in each realization. Since the stacked signals over ~ 10 voids are quite weak, it is difficult to discuss the impact of $f(R)$ gravity on the stacked signals for each 25 deg^2 . Therefore, we decide to measure the stacked signal using all voids in 100 realizations. The error bars of the stacked signals at the angular separation of θ are simply estimated by summing up the error which obtained from void profiles and LSS, and shape noise

$$\sigma_{\gamma_+}^2 = \sigma_{\text{void}}^2 + \sigma_{\text{LSS}}^2 + \frac{\sigma_e^2}{2n_{\text{gal}}} \left\{ \frac{1}{N_{\text{stack}}(2\pi\theta\Delta\theta)} \right\}, \quad (50)$$

where N_{stack} represents the number of objects used for stacked analysis and $\Delta\theta$ is the bin size of angular separation. σ_{void} and σ_{LSS} are errors from dark matter distributions around voids and large-scale structure on the line of sight, which are estimated from a covariance matrix with Eq.(11) in Higuchi et al. (2013). We here consider the 25 bins of angular separation in the range of 0-200 arcmin with $\Delta\theta = 8 \text{ arcmin}$.

Figure 4 shows the results of void stacking in each void radius bin as a function of distance from a center of a void. The error bar shown in this figure corresponds to the statistical uncertainty for a 2500 deg^2 survey. Clearly, it is difficult to find any effects on $f(R)$ gravity on the stacked signals around voids. In order to evaluate the profile quantitatively, we fit the profiles with void model as shown in Section 3.2.1. Table 1 shows the results of fitting with the double top-hat model. The 1σ uncertainty of fitting parameters in Table 1 are estimated with boot strap method. We select voids randomly, stack and measure the stacked profile over selected voids. We then make 100 stacked profiles for a given void radius bin and calculate the standard deviation over 100 profiles. We perform the profile fitting by using Eq. (27) with three fitting parameters: density contrast of a void δ_1 , size of a void θ_1 and size of a ridge θ_2 . In the fitting, lens redshift is set to be $z_l = 0.4$. We cannot find significant difference between estimated parameters, indicating that profiles are same within errors.

Cai et al. (2015) finds that stacking voids can constrain $f(R)$ gravity down to F5 with a Gpc scale survey. In our analysis,

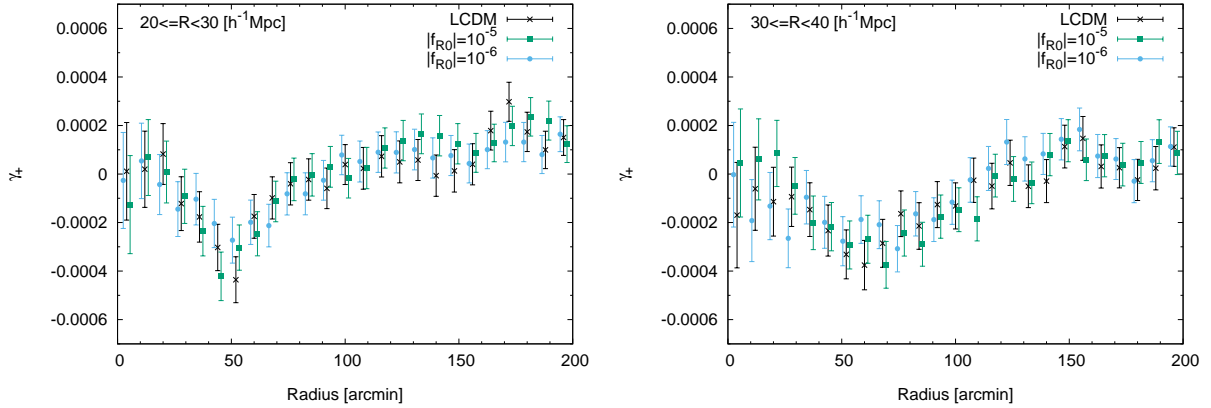


Figure 4. Stacked tangential shear profiles around voids for two bins of void radius R . The horizontal axis shows angular distance from a center of a void. Crosses, squares and circles show the profiles for Λ CDM, $|f_{R0}| = 10^{-5}$ and $|f_{R0}| = 10^{-6}$, respectively. The error bars represent the statistical uncertainty related to the shape noise for a sky coverage of 2500 deg^2 . *Left:* $20 \leq R [h^{-1}\text{Mpc}] < 30$, *Right:* $30 \leq R [h^{-1}\text{Mpc}] < 40$

Table 1. Results of the fitting with the double top-hat model. The lens redshift is set to be 0.4. Errors show 1σ estimated with bootstrap method. Column (1): cosmological model, Column(2)-(3): fitting result. The unit of θ_1 and θ_2 is arcmin.

model \ radius [$h^{-1}\text{Mpc}$]	20 – 30	30 – 40
Λ CDM	$\delta_1 = -0.512 \pm 0.135$	$\delta_1 = -0.472 \pm 0.119$
	$\theta_1 = 47.0 \pm 3.01$	$\theta_1 = 53.7 \pm 7.12$
	$\theta_2 = 81.6 \pm 29.5$	$\theta_2 = 122 \pm 34.7$
$ f_{R0} = 10^{-5}$	$\delta_1 = -0.688 \pm 0.153$	$\delta_1 = -0.475 \pm 0.158$
	$\theta_1 = 40.9 \pm 3.46$	$\theta_1 = 57.9 \pm 10.6$
	$\theta_2 = 85.2 \pm 18.4$	$\theta_2 = 131 \pm 21.2$
$ f_{R0} = 10^{-6}$	$\delta_1 = -0.413 \pm 0.168$	$\delta_1 = -0.363 \pm 0.231$
	$\theta_1 = 50.0 \pm 9.49$	$\theta_1 = 64.0 \pm 17.5$
	$\theta_2 = 90.7 \pm 13.8$	$\theta_2 = 112 \pm 22.0$

on the other hand, it is difficult to find large differences between cosmological models for each size of voids. This discrepancy mainly comes from the difference between stacking methods and the number of voids used in the stacking analysis. They use more than 10^4 voids for the stacking while we only use 10^3 voids at most. When their errors are scaled with the number of voids used in this paper, the errors are increased by more than three times. Therefore, one can not distinguish the profiles between $f(R)$ and Λ CDM when also using their simulation. This result is consistent with our result which includes more realistic effects by using ray-tracing simulations. As a result, stacked void lensing is a promising tool for giving constraint on $f(R)$ in future large-scale survey. However, larger surveys such as LSST (Ivezic et al. 2008) are required.

5.1.3 Troughs

In this section, we evaluate the effects of $f(R)$ gravity on the stacked signal around troughs. We estimate the error bars of tangential shear by the standard deviation over 100 realizations and take into account the contribution from shape noise by using third term in Eq. (50). Note that the errors represent the uncertainty with the sky coverage of 25 square degrees.

We first compare the simulation results in the Λ CDM model with the theoretical model in Gruen et al. (2016). Figure 5 summarizes the results in the case of the halo catalog with the mass threshold of $M_T = 10^{13} h^{-1} M_\odot$. We consider the four cases of trough radius $\theta_T = 5, 10, 20$ and 30 arcmin. The black point in Figure 5 represents the average stacked signals $\langle \gamma_+ \rangle$ over 100 realizations, while the red line corresponds to the theoretical model. We find that the model in Gruen et al. (2016) provides the reasonable fit to the simulation results for $M_T = 10^{13} h^{-1} M_\odot$ and different four trough radiuses. However, the measured signals around troughs would be strongly affected by the selection criteria of halo masses. Figure 6 shows the dependence of M_T on the stacked signals around the troughs in the case of Λ CDM. The left panel in Figure 6 summarizes the results of $\langle \gamma_+ \rangle$ in the case of $\theta_T = 5$ arcmin, while the right one corresponds to the average convergence profile $\langle \kappa \rangle$. We find that the expected profiles as shown in Gruen et al. (2016) are observed only when we set to be $M_T = 10^{13} h^{-1} M_\odot$ in our simulations. Convergence profiles with large halo mass criteria tend to show positive values while this trend appears for lower mass selection criteria. This might be caused by the presence of massive halos with mass of $M < M_T$ in a trough radius. However, this effect is found to be smaller as the trough radius increases.

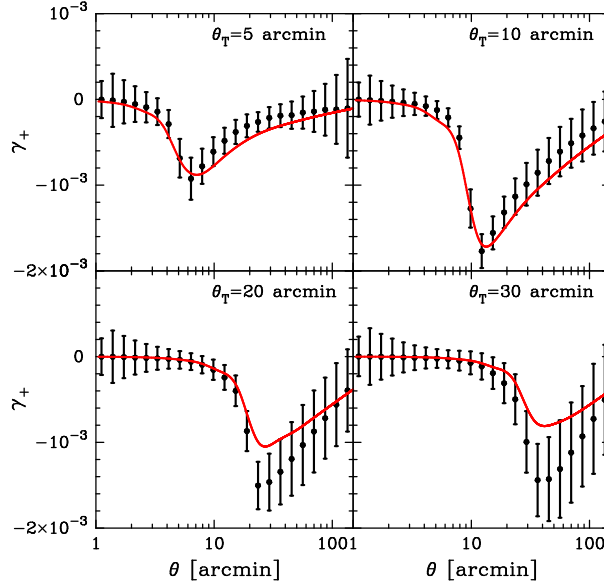


Figure 5. The comparison between the measured stacked signals around troughs from 100 Λ CDM simulations and the theoretical prediction in Section 3.2.1. We consider the troughs selected from the halo catalogs with $M_T = 10^{13} h^{-1} M_\odot$. The black point shows the average stacked signal over 100 realizations and the error bars show the standard deviations estimated from 100 maps. The red line represents the theoretical model as proposed in Gruen et al. (2016).

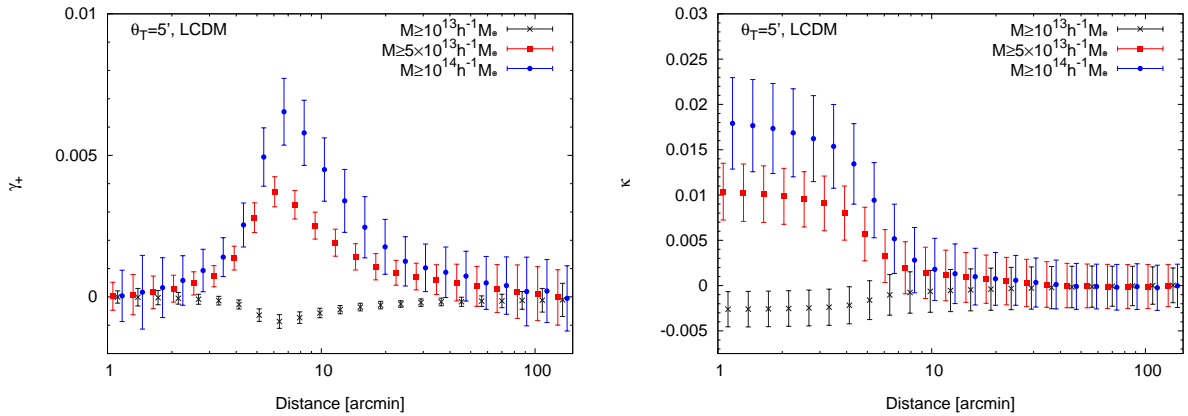


Figure 6. Stacked signals around troughs with $\theta_T = 5'$ in the Λ CDM model when we apply the different halo mass criteria. Crosses, squares and circles show the profiles with mass criteria $M_T = 10^{13} h^{-1} M_\odot$, $5 \times 10^{13} h^{-1} M_\odot$ and $10^{14} h^{-1} M_\odot$. *Left:* tangential shear profile, *Right:* convergence profile.

We then consider the imprint of $f(R)$ gravity on the stacked signals around troughs. Figure 7 shows the stacked tangential shear profiles for the Λ CDM and two $f(R)$ models. As seen in this figure, we can find the differences of $\langle \gamma_+ \rangle$ at $\theta \sim \theta_T$ between the F5 model and Λ CDM model when using the troughs with $\theta_T = 5$ arcmin and the halo catalogs with $M_T = 10^{13} h^{-1} M_\odot$. In order to define the significance with the more quantitative manner, we introduce the significance level of the difference between the two models of tangential shear profile $\gamma_{+, (a)}$ and $\gamma_{+, (b)}$ for each bin as follows:

$$(S/N)^2 = \sum_i \frac{[\gamma_{+, (a)}(\theta_i) - \gamma_{+, (b)}(\theta_i)]^2}{\sigma^2 N_{bin}^2}, \quad (51)$$

where σ represents the statistical uncertainty in stacked analysis for a given sky coverage. In order to calculate Eq. (51) for the troughs with $\theta_T = 5$ arcmin and $M_T = 10^{13} h^{-1} M_\odot$, we consider 23 bins in the range of 1-150 arcmin and compute the standard deviation of stacked signals over 100 Λ CDM simulations. We then use this standard deviation as the estimator of σ in a 25 deg^2 sky. Assumed that σ would be scaled with survey area, we find that the signal-to-noise ratio between the F5 model and Λ CDM model would be 1.43 for each bin in a sky coverage of $1,400 \text{ deg}^2$ as proposed in the ongoing Subaru/Hyper Suprime-Cam (HSC) survey (Miyazaki et al. 2006). Therefore, we conclude that the stacked signal around troughs can be useful to distinguish the $f(R)$ model with $|f_{R0}| = 10^{-5}$ and the standard Λ CDM model with a $\sim 2\sigma$ level in the ongoing

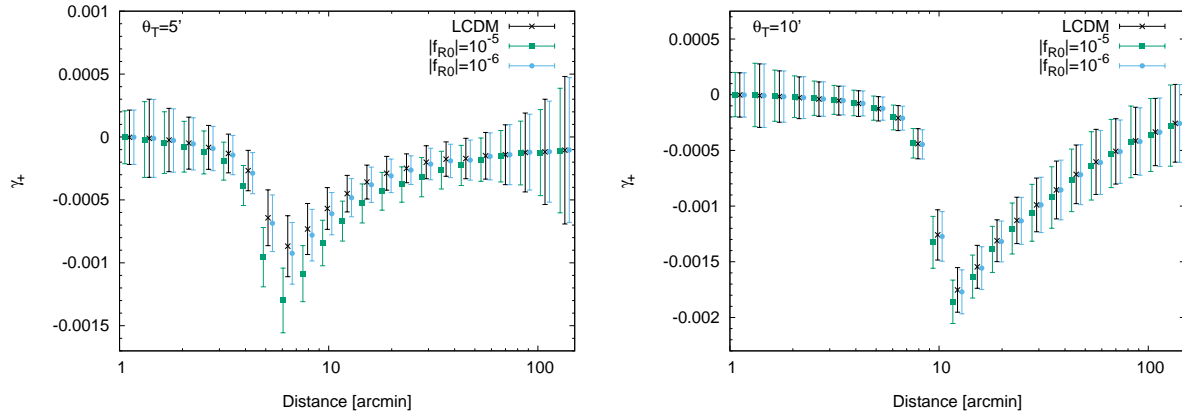


Figure 7. Stacked profiles of troughs for two bins of trough radius. We set halo masses to be $M_T = 10^{13} h^{-1} M_\odot$ for the selection of troughs. Crosses, squares and circles show the profiles for Λ CDM, $|f_{R0}| = 10^{-5}$ and $|f_{R0}| = 10^{-6}$. *Left:* $\theta_T = 5$ arcmin, *Right:* $\theta_T = 10$ arcmin

large-scale survey. Note that we cannot observe any significant differences of tangential shear between the F5 model and Λ CDM model over 100 realizations for a set of M_T and θ_T , except for the case of $\theta_T = 5$ arcmin and $M_T = 10^{13} h^{-1} M_\odot$. Moreover, we cannot find any significant differences between the stacked profile around troughs in the F6 model and the Λ CDM model in our simulations.

5.2 Peak Statistics

In this section, we simulate galaxy shape noise in our simulation by adding the shape noise to shear from random ellipticities which follow the two-dimensional Gaussian distribution as

$$P(|e|) = \frac{1}{\pi\sigma_{\text{int}}^2} \exp\left(-\frac{e^2}{\sigma_{\text{int}}^2}\right), \quad (52)$$

where $\sigma_{\text{int}}^2 = \sigma_e^2 / (n_{\text{gal}} \theta_{\text{pix}}^2)$ with the pixel size of $\theta_{\text{pix}} = 0.075$ arcmin. When analyzing the peaks, we remove the regions within smoothing scale θ_G from edges of each convergence map.

5.2.1 Peak-Halo matching

We first examine the correspondence between dark matter haloes and the local maximum in smoothed convergence map. With our ray-tracing simulations and mock halo catalogs, we study the correspondence between haloes and the peaks in weak lensing convergence maps. We first identify the local maxima in the smoothed convergence field with source redshift of $z_{\text{source}} = 1$. For selection of peaks, the threshold of peak height is set to be $\mathcal{K} = 0.04$ for noise-less maps and 0.06 for noisy maps. These value correspond to $\sim 3\sigma$ in smoothed convergence maps without and with noise, respectively. For a given position of lensing peak, we search for the matched dark matter haloes within a radius of 3 arcmin from the peak position. This search radius is set to be larger than the smoothing scale but still smaller than the angular size of massive haloes at $z \sim 0.1 - 0.7$ (also see, Hamana et al. 2004). When we find several haloes in search radius, we regard the matched halo as the closest halo from the position of peak. For each matched peak, we estimate the corresponding convergence by using the universal NFW density profile (Eq. 18). In the calculation of expected convergence from haloes, we convert the mass defined by $M = 4\pi/3 \times 200\bar{\rho}_m R_{200}^3$ to the virial mass by using the halo concentration shown in Eq. (19). In total, for the Λ CDM cosmology, we find 25,806 and 12,865 pairs of peaks and haloes over 100 noise-less maps and noisy maps.

The left panels of Figure 8 shows the scatter plot of peak height in convergence map and the expected convergence by NFW haloes in the case of the Λ CDM cosmology. The vertical axis corresponds to peak height, while the horizontal axis shows the corresponding convergence expected by NFW haloes. Thus, the colour map in each panel shows the probability of $\text{Prob}(\mathcal{K}_{\text{peak,obs}}|\mathcal{K}_{\text{peak,h}})$. We present the line of $y = x$ as the dashed line in each panel. In lower panel, we show the effect of the modulation of peak height as the magenta line with error bars. The magenta line represents $\langle \mathcal{K}_{\text{peak,obs}}|\mathcal{K}_{\text{peak,h}} \rangle$, which is defined by

$$\langle \mathcal{K}_{\text{peak,obs}}|\mathcal{K}_{\text{peak,h}} \rangle(z, M) = \int d\mathcal{K} \mathcal{K} \text{Prob}(\mathcal{K}|\mathcal{K}_{\text{peak,h}}(z, M)) \quad (53)$$

and the error bars reflect the scatter of $\langle \mathcal{K}_{\text{peak,obs}}|\mathcal{K}_{\text{peak,h}} \rangle$. As shown in previous works, we confirm the good correspondence between the matched dark matter haloes and lensing peaks in the noise-less maps. Nevertheless, even in the noise-less maps,

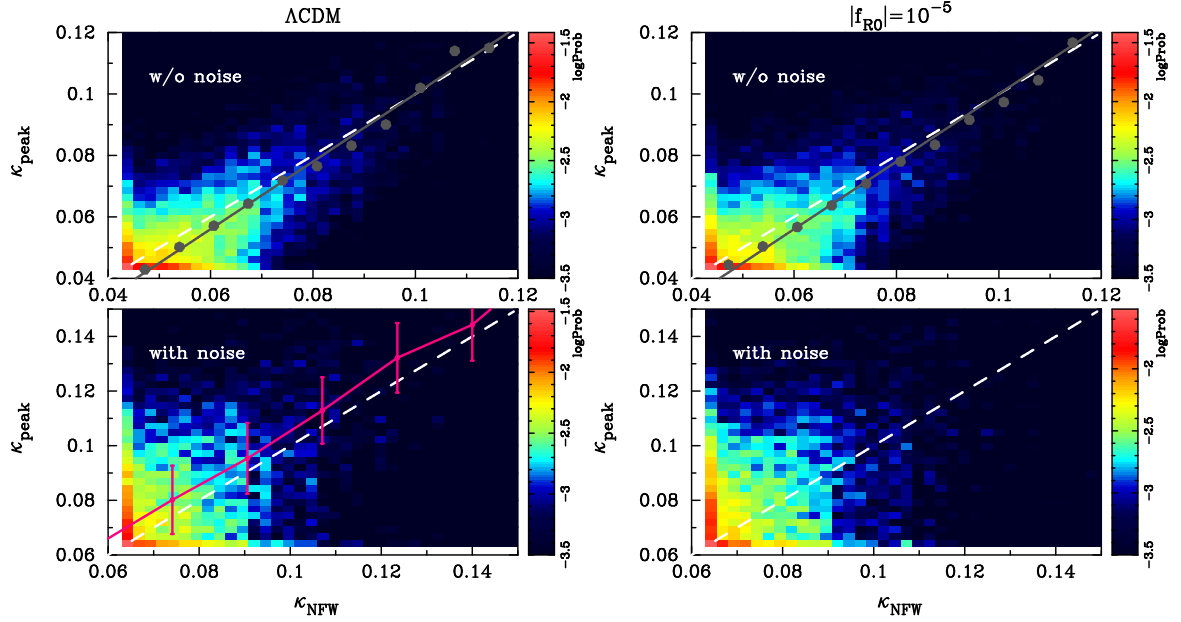


Figure 8. The correspondence between dark matter haloes and lensing peaks. In each panel, the vertical axis represents the peak height and the horizontal axis shows the expected convergence of NFW haloes. In both right and left panels, the top panel shows the scatter plot of peak height and the expected convergence by the matched haloes in absence of noise, while the lower panel corresponds to the case with shape noise. *Left:* The Λ CDM model. *Right:* $f(R)$ model with $|f_{R0}| = 10^{-5}$.

the better correspondence between the matched haloes and peaks would be generalized by (Shirasaki et al. 2015)

$$\mathcal{K}_{\text{peak,obs}}(z, M) = c_0 + c_1 \mathcal{K}_{\text{peak,h}}(z, M). \quad (54)$$

In the top left panel of Figure 8, the gray line shows Eq. (54) with $c_0 = -0.01$ and $c_1 = 1.1$ and the gray point represents $\langle \mathcal{K}_{\text{peak,obs}} | \mathcal{K}_{\text{peak,h}} \rangle$ measured from the simulation results. Also, our model as shown in Eq. (53) can explain the average relation between peaks and dark matter haloes even in the case with noise.

We also perform the similar calculations in the F5 model. We simply assume the NFW profile with the halo concentration expressed by Eq. (19) in the case of non-zero $|f_{R0}|$. In the F5 model, we find 29,767 and 14,410 pairs of peaks and haloes over 100 noise-less maps and noisy maps, respectively. The right panels in Figure 8 correspond to the case of the F5 model. Compared to the left panels, we cannot find any significant impact on $f(R)$ gravity on the correspondence between haloes and peaks in both noise-less maps and noisy maps. In the right top panel, we again show measured $\langle \mathcal{K}_{\text{peak,obs}} | \mathcal{K}_{\text{peak,h}} \rangle$ from the pairs of haloes and peaks by the gray points, while the gray line represents Eq. (54) with $c_0 = -0.01$ and $c_1 = 1.1$. Thus, the probability of $\text{Prob}(\mathcal{K}_{\text{peak,obs}} | \mathcal{K}_{\text{peak,h}})$ is less affected by the modification of gravity for the HS model with $|f_{R0}| \lesssim 10^{-5}$. This result is consistent with the result shown in Figure 3 because the expected peak height for a given NFW halo $\mathcal{K}_{\text{peak,h}}$ would be determined mainly by the tangential shear profile at $\theta \sim 2 - 3\theta_G$, where the effect of $f(R)$ gravity should be less than 10%.

5.2.2 Abundance of high significance local maxima

We then consider the abundance of local maxima with high height, which is expected to be associated with single massive dark matter halo along a line of sight. As shown in Figure 8, the probability distribution function of observed peak height for a given matched dark matter halo is less affected by the modification of gravity. This implies that the number count of high significance local maxima can be useful to extract information about the number density of dark matter haloes, or the halo mass function.

Assumed that the halo density profile would not be affected by the modification of gravity, we can predict the abundance of high significance local maxima as shown in Section 3.2.2. Figure 9 shows the comparison between measured abundance from 100 ray-tracing simulations and our model. In both left and right panels, the red points with error bars represent the number count of local maxima in the noisy maps, while the blue is for the noise-less maps. The error bars correspond to the standard deviation over 100 realizations. Also, the dashed and solid lines are our model for the noisy and noise-less cases, respectively.

As shown in this figure, our model can provide the good fit to simulation results in the standard Λ CDM models, regardless of the presence or absence of shape noise. For the $f(R)$ model, we compute the mass function with the *corrected* mass variance,

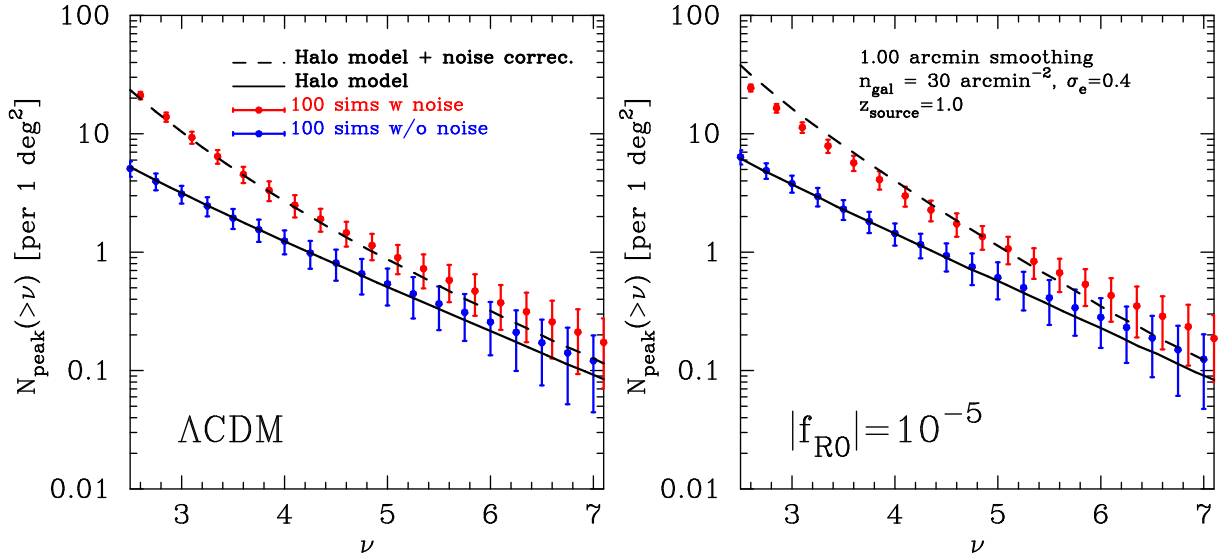


Figure 9. The comparison of abundance of local maxima measured in simulations and the halo model prediction. In both panels, the red points with error bars represent the results in 100 noisy maps, while the blue is for the noise-less maps. The solid and dashed lines are our model with and without shape noises, respectively. *Left:* The Λ CDM model. *Right:* $f(R)$ model with $|f_{R0}| = 10^{-5}$.

which is given by (Li & Hu 2011)

$$\sigma(M) = \frac{\sigma_{f(R)}(M) + (M/M_{\text{th}})^p \sigma_{\Lambda\text{CDM}}}{1 + (M/M_{\text{th}})^p}, \quad (55)$$

where $\sigma_{f(R)}$ is the mass variance with the linear matter power spectrum in the $f(R)$ model and $\sigma_{\Lambda\text{CDM}}$ is the mass variance in the ΛCDM model. The transition mass scale M_{th} and the parameter p are found to be $M_{\text{th}} = 1.345 \times 10^{13} h^{-1} M_{\odot} (|f_{R0}|/10^{-6})^{3/2}$ and $p = 2.448$ in Li & Hu (2011). We take Eq. (55) and simply adopt the functional form of mass function calibrated in Tinker et al. (2008). Note that we have confirmed that this is a reasonable approximation in our halo catalogs with $M_{200} \geq 10^{13} h^{-1} M_{\odot}$ and the redshift of 0-1. Under these assumption, we can compare the abundance of high significance peaks with our model prediction and then find that the our model works even in the F5 model for both noisy and noise-less maps.

5.2.3 General peak count and its cosmological application

As summarized in Section 3.2.2, peaks can be defined by local maxima or minima in the smoothed convergence map in general. In this section, we examine the effect on $f(R)$ gravity on number count of local maxima and minima by using 100 ray-tracing simulations. We estimate the statistical uncertainty of peak counts in a 25 deg^2 area from the standard deviation over 100 realizations. For the statistical uncertainty in the ongoing HSC survey with the sky coverage of 1400 deg^2 , we scale the uncertainty with the sky coverage (i.e., by a factor of $\sqrt{1400/25}$).

The left panel in Figure 10 shows the number count of peaks with the smoothing scale $\theta_G = 1 \text{ arcmin}$ and $\theta_o = 10 \text{ arcmin}$, while the right corresponds to the ratio of the number of peaks between the $f(R)$ model and the ΛCDM model. The peak height ν are binned into 40 bins from -10 to 10 linearly. For the HS model with $|f_{R0}| = 10^{-5}$, we find that the number of peaks with the $\nu \gtrsim 3$ would increase with a level of $\sim 30\%$ compared to the ΛCDM model. Interestingly, the number of peaks with $\nu \lesssim -2$ would be also affected by the presence of the fifth force, increasing the number of peaks by a factor of ~ 1.5 . Since negative peaks are caused by superposition of underdense regions on line of sight, increasing the number of voids in $f(R)$ gravity might affect the number count of negative peaks. On the other hand, we cannot find any significant deviations in peak counts for $|f_{R0}| = 10^{-6}$.

Let us quantify the significance of the differences shown in Figure 10 by introducing the following statistic

$$\left(\frac{S}{N}\right)_{\text{peak}}^2 = \sum_i \left(\frac{N_{\text{peak},i}^{|f_{R0}|} - N_{\text{peak},i}^{\Lambda\text{CDM}}}{\sigma_{\text{peak},i}} \right)^2, \quad (56)$$

where $N_{\text{peak},i}^{|f_{R0}|}$ represents the number count of i -th bin for the model with the parameter of $|f_{R0}|$, $\sigma_{\text{peak},i}$ is the statistical uncertainty of the number count of i -th bin for ΛCDM . Note that $N_{\text{peak},i}^{\Lambda\text{CDM}}$ corresponds to the case of ΛCDM . Table 2 shows the result of signal-to-noise ratio. In the estimation, we do not use high peaks whose number count is zero. The significance for the F5 model becomes more than 1σ as average value in each bin.

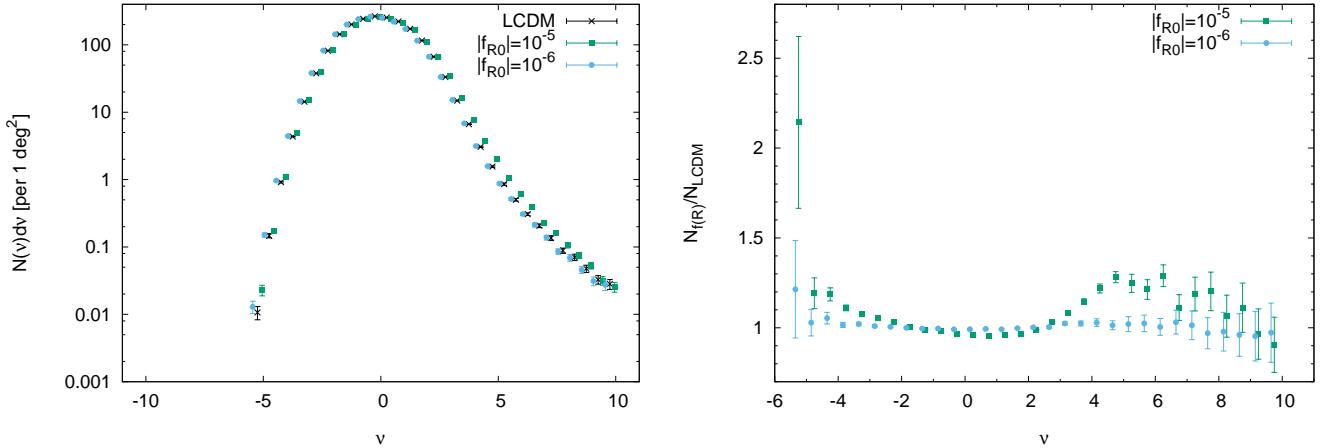


Figure 10. Comparison of the number count of peaks for each cosmological model. The horizontal axis shows the peak height normalized by the shape noise variance. In both panels, we consider the number count of local maxima and minima in a convergence map with the bin size of $\Delta\nu = 0.5$. In the left panel, crosses, squares and circles show the number of lensing peaks for Λ CDM, $|f_{R0}| = 10^{-5}$ and $|f_{R0}| = 10^{-6}$, respectively. The right panel represents the ratio of the number counts for the $f(R)$ model normalized by that in the Λ CDM. The error bars correspond to the statistical uncertainty for the ongoing HSC survey with the sky coverage of 1400 deg².

Table 2. Total S/N which indicates difference of the number count of peaks between Λ CDM and $f(R)$. Error bars are estimated with 100 realizations and scaled for the HSC survey. Column (1): cosmological model, Column(2): values of peaks ν used for the estimation

$f(R)$ model	$-10 \leq \nu \leq 10$ (31 bins)	$ \nu \geq 4$ (15 bins)
$ f_{R0} = 10^{-5}$	39.39	20.81
$ f_{R0} = 10^{-6}$	7.269	2.770

6 CONCLUSION AND DISCUSSION

We have studied the matter density distribution in $f(R)$ gravity. In particular, we have focused on the large-scale structures which can be observed in weak lensing measurement. We have performed ray-tracing simulations in two different $f(R)$ gravity models and the standard Λ CDM model. Using a set of weak lensing maps and dark matter halo catalogs, we have investigated the connection with observables and large-scale structures in a realistic way. Throughout this paper, we have considered two different statistical methods and compared the statistics in the standard Λ CDM model with the $f(R)$ model proposed in [Hu & Sawicki \(2007\)](#). Our main findings are summarized as follows:

(i) The averaged tangential shear profile around dark matter haloes shows a clear dependence on $f(R)$ gravity. The significant deviation from Λ CDM is found at *both* the inner region and the outskirts of dark matter haloes. The trend of deviation would depend on the halo masses and redshifts in a non-monotonic way.

(ii) While the averaged tangential shear profile around voids is expected to be a promising target to probe the modification of gravity, we cannot find any significant differences between the $f(R)$ model and Λ CDM model even if using ~ 1000 voids. This result indicates that the uncertainty of the center of voids and the projected matter distribution along a line of sight would mitigate the effect of $f(R)$ gravity on the signal around voids. However, larger surveys would be able to distinguish profiles between Λ CDM and $f(R)$ gravity.

(iii) Troughs, the underdense regions in the surface density field of galaxies, are proposed as the tracer of the underdensity in the Universe. In this paper, we consider the troughs defined by dark matter haloes and examine how the tangential shear profile around troughs would be affected by the modification of gravity. The stacked tangential shear profile around troughs clearly shows the contribution from the underdensity in the Universe. The clear deviation from Λ CDM have been confirmed when the angular separation would be equal to the search radius of troughs. However, we also find that correct understanding of halo catalogs would be required in order to sample the underdense regions in the Universe with troughs.

(iv) Peaks in a reconstructed mass map from weak lensing measurement can in principle contain the cosmological information about dark matter haloes, voids and structures along a line of sight. We perform matching analysis of local maximum in a map to dark matter halo along the line of sight. We then confirm that the clear correspondence between local maxima and haloes in absence of shape noises and the modulation effect in the relation of maxima and haloes for noisy maps. There-

fore, proper understanding of the relation of maxima and haloes enables us to extract the information about the halo mass function. We demonstrate the number count of local maxima can be explained by the combination of the halo mass function and the correspondence between maxima and haloes. Furthermore, the number count of local minima would bring additional information about the modification of gravity.

(v) Throughout this paper, we consider the two models of $f(R)$ gravity with the degree of freedom of a new scalar field $|f_{R0}| = 10^{-5}$ and 10^{-6} . We find that the stacked analysis around troughs and peak number counts can constrain on the model with $|f_{R0}| = 10^{-5}$ with $\sim 2\sigma$ level, assumed ongoing imaging surveys with the sky coverage of a several thousands squared degrees. On the other hand, it is challenging to constrain the model with $|f_{R0}| = 10^{-6}$ with our proposed statistical methods.

Although our findings would play an essential role to understand the nature of gravity with weak lensing measurement, there are several caveats and limitations that must be kept in mind when interpreting the results presented in this work.

First, the simulation in this paper does not include any baryonic physics and the possible effect due to the presence of massive neutrinos. Both baryonic physics model and massive neutrinos can affect the cosmic structure formation in various length scales. (e.g., [Duffy et al. 2010](#); [Cui et al. 2012](#); [Massara et al. 2014](#); [Castorina et al. 2015](#)). In particular, our results on stacked signals around haloes (Section 5.1.1) would potentially be affected by the baryonic physics at the inner regions, while the massive neutrinos might have some impacts on the signals at the outskirts of each dark matter halo. The simplest way to quantify these effects is to get together all effects simultaneously: to run cosmological hydrodynamical simulation under the modified gravity (e.g., [Puchwein et al. 2013](#)) in the presence of massive neutrinos.

There exist other statistical methods of weak lensing to extract cosmological information about the modification of gravity. For instance, the two-point correlation of cosmic shear (or power spectrum) has been proposed in previous works (e.g., [Heavens et al. 2007](#)) and applied to existing data set (e.g., [Harnois-Déraps et al. 2015](#)). Moreover, higher-order correlation function (e.g., [Gil-Marín et al. 2011](#)) and morphological statistics ([Ling et al. 2015](#)) would be useful to improve the constraints on the nature of gravity in weak lensing surveys. Since our simulations can be helpful to understand the cosmological information content of weak lensing statistics, we plan to study them in details in future ([Shirasaki et al. in prep](#)).

On the stacked analysis with voids, we should note that only ~ 10 voids are found in each realization of our simulation. In addition, we might underestimate the errors due to the limitation of simulation size. Thus, larger weak lensing simulation would be more important to characterize the statistical property of cosmic voids and improve our understanding of the stacked signals around voids under the modified gravity. For this purpose, the full-sky simulation of weak gravitational lensing (e.g., [Shirasaki et al. 2015](#)) would be suitable to increase the sample size of voids and haloes. A larger sample of voids and haloes would also enable us to study the mass assembly history in the modified gravity theory.

ACKNOWLEDGMENTS

We thank an anonymous referee for careful reading and suggestion to improve the article. We would like to thank Baojiu Li for useful discussions and comments. M.S. is supported by Research Fellowships of the Japan Society for the Promotion of Science (JSPS) for Young Scientists. Numerical computations presented in this paper were in part carried out on the general-purpose PC farm at Center for Computational Astrophysics, CfCA, of National Astronomical Observatory of Japan. Data analysis were [in part] carried out on common use data analysis computer system at the Astronomy Data Center, ADC, of the National Astronomical Observatory of Japan.

REFERENCES

- Achitouv I., Baldi M., Puchwein E., Weller J., 2015, preprint (arXiv:1511.01494),
 Arnold C., Puchwein E., Springel V., 2014, *MNRAS*, **440**, 833
 Bartelmann M., Schneider P., 2001, *Physical Rep.*, **340**, 291
 Bean R., Bernat D., Pogosian L., Silvestri A., Trodden M., 2007, *Phys. Rev. D*, **75**, 064020
 Bertschinger E., 1995, preprint (arXiv:9506070),
 Bose S., Hellwing W. A., Li B., 2015, *JCAP*, **2**, 034
 Brax P., van de Bruck C., Davis A.-C., Khoury J., Weltman A., 2004, *Phys. Rev. D*, **70**, 123518
 Cai Y.-C., Padilla N., Li B., 2015, *MNRAS*, **451**, 1036
 Castorina E., Carbone C., Bel J., Sefusatti E., Dolag K., 2015, *JCAP*, **7**, 043
 Clampitt J., Cai Y.-C., Li B., 2013, *MNRAS*, **431**, 749
 Cui W., Borgani S., Dolag K., Murante G., Tornatore L., 2012, *MNRAS*, **423**, 2279
 Dietrich J. P., Hartlap J., 2010, *MNRAS*, **402**, 1049
 Duffy A. R., Schaye J., Kay S. T., Dalla Vecchia C., Battye R. A., Booth C. M., 2010, *MNRAS*, **405**, 2161
 Dutton A. A., Macciò A. V., 2014, *MNRAS*, **441**, 3359
 Fan Z., Shan H., Liu J., 2010, *ApJ*, **719**, 1408
 Foster C., Nelson L. A., 2009, *ApJ*, **699**, 1252
 Gil-Marín H., Schmidt F., Hu W., Jimenez R., Verde L., 2011, *JCAP*, **11**, 019

- Gruen D., et al., 2016, *MNRAS*, **455**, 3367
- Hamana T., Mellier Y., 2001, *MNRAS*, **327**, 169
- Hamana T., Takada M., Yoshida N., 2004, *MNRAS*, **350**, 893
- Hammami A., Llinares C., Mota D. F., Winther H. A., 2015, *MNRAS*, **449**, 3635
- Harnois-Déraps J., Munshi D., Valageas P., van Waerbeke L., Brax P., Coles P., Rizzo L., 2015, *MNRAS*, **454**, 2722
- He J.-h., Li B., Jing Y. P., 2013, *Phys. Rev. D*, **88**, 103507
- Heavens A. F., Kitching T. D., Verde L., 2007, *MNRAS*, **380**, 1029
- Higuchi Y., Oguri M., Hamana T., 2013, *MNRAS*, **432**, 1021
- Hoyle F., Vogeley M. S., 2004, *ApJ*, **607**, 751
- Hoyle F., Rojas R. R., Vogeley M. S., Brinkmann J., 2005, *ApJ*, **620**, 618
- Hu W., Kravtsov A. V., 2003, *ApJ*, **584**, 702
- Hu W., Sawicki I., 2007, *Phys. Rev. D*, **76**, 064004
- Ivezic Z., et al., 2008, preprint (arXiv:0805.2366),
- Kaiser N., 1992, *ApJ*, **388**, 272
- Khoury J., Weltman A., 2004a, *Phys. Rev. D*, **69**, 044026
- Khoury J., Weltman A., 2004b, *Phys. Rev. Lett.*, **93**, 171104
- Kratochvil J. M., Haiman Z., May M., 2010, *Phys. Rev. D*, **81**, 043519
- Li Y., Hu W., 2011, *Phys. Rev. D*, **84**, 084033
- Li B., Zhao G.-B., Koyama K., 2012a, *MNRAS*, **421**, 3481
- Li B., Zhao G.-B., Teyssier R., Koyama K., 2012b, *JCAP*, **1201**, 051
- Limber D. N., 1954, *ApJ*, **119**, 655
- Ling C., Wang Q., Li R., Li B., Wang J., Gao L., 2015, *Phys. Rev. D*, **92**, 064024
- Marian L., Smith R. E., Angulo R. E., 2015, *MNRAS*, **451**, 1418
- Martinelli M., Melchiorri A., Mena O., Salvatelli V., Gironés Z., 2012, *Phys. Rev. D*, **85**, 024006
- Massara E., Villaescusa-Navarro F., Viel M., 2014, *JCAP*, **12**, 053
- Miyazaki S., et al., 2006, in Society of Photo-Optical Instrumentation Engineers (SPIE) Conference Series. , doi:10.1117/12.672739
- Navarro J. F., Frenk C. S., White S. D. M., 1997, *ApJ*, **490**, 493
- Nojiri S., Odintsov S. D., 2011, *Physical Rep.*, **505**, 59
- Oguri M., Takada M., 2011, *Phys. Rev. D*, **83**, 023008
- Oyaizu H., Lima M., Hu W., 2008, *Phys. Rev. D*, **78**, 123524
- Pan D. C., Vogeley M. S., Hoyle F., Choi Y.-Y., Park C., 2012, *MNRAS*, **421**, 926
- Perlmutter S., et al., 1997, *ApJ*, **483**, 565
- Planck Collaboration et al., 2015, preprint (arXiv:1502.01589),
- Prunet S., Pichon C., Aubert D., Pogosyan D., Teyssier R., Gottloeber S., 2008, *Astrophys. J. Suppl.*, **178**, 179
- Puchwein E., Baldi M., Springel V., 2013, *MNRAS*, **436**, 348
- Sato M., Hamana T., Takahashi R., Takada M., Yoshida N., Matsubara T., Sugiyama N., 2009, *ApJ*, **701**, 945
- Schmidt F., Lima M., Oyaizu H., Hu W., 2009, *Phys. Rev. D*, **79**, 083518
- Schneider P., Seitz C., 1995, *A&A*, **294**, 411
- Sheth R. K., van de Weygaert R., 2004, *MNRAS*, **350**, 517
- Shi D., Li B., Han J., Gao L., Hellwing W. A., 2015, *MNRAS*, **452**, 3179
- Shirasaki M., Hamana T., Yoshida N., 2015, *MNRAS*, **453**, 3043
- Shirasaki M., Hamana T., Yoshida N., 2016, *PASJ*, **68**, 4
- Tegmark M., et al., 2006, *Phys. Rev. D*, **74**, 123507
- Tessore N., Winther H. A., Metcalf R. B., Ferreira P. G., Giocoli C., 2015, *jcap*, **10**, 036
- Tinker J. L., Kravtsov A. V., Klypin A., Abazajian K., Warren M. S., et al., 2008, *ApJ*, **688**, 709
- Tinker J. L., Robertson B. E., Kravtsov A. V., Klypin A., Warren M. S., et al., 2010, *ApJ*, **724**, 878
- Vainshtein A. I., 1972, *Phys. Lett. B*, **39**, 393
- White M., Hu W., 2000, *ApJ*, **537**, 1
- Yang X., Kratochvil J. M., Wang S., Lim E. A., Haiman Z., May M., 2011, *Phys. Rev. D*, **84**, 043529
- Zhao G.-B., 2014, *ApJS*, **211**, 23
- Zhao G.-B., Li B., Koyama K., 2011, *Phys. Rev. D*, **83**, 044007
- Zivick P., Sutter P. M., Wandelt B. D., Li B., Lam T. Y., 2015, *MNRAS*, **451**, 4215
- de La Cruz-Dombriz A., Dobado A., Maroto A. L., 2008, *Phys. Rev. D*, **77**, 123515